Characterization of commercially cold sprayed copper coatings and determination of the effects of impacting copper powder velocities

P. Jakupi [a], P.G. Keech [b], I. Barker [c], S. Ramamurthy [d], R.L. Jacklin [d], D.W. Shoesmith [d, *], D.E. Moser [c]

[a] Western University, Dept. of Chemistry, London Ontario, N6A 3K7, Canada
[b] Nuclear Waste Management Organization, 22 St. Clair Ave. E., Toronto Ontario, M4T 2S3, Canada
[c] Western University, Dept. of Earth Sciences, London Ontario, N6A 3K7, Canada
[d] Western University, Surface Science Western, 999 Collip Circle, LL31 (Lower), London, Ontario, N6G OJ3, Canada

ABSTRACT

Copper coated steel containers are being developed for the disposal of high level nuclear waste using processes such as cold spray and electrodeposition. Electron Back-Scatter Diffraction has been used to determine the microstructural properties and the quality of the steel-copper coating interface. The influence of the nature of the cold-spray carrier gas as well as its temperature and pressure (velocity) on the coating's plastic strain and recrystallization behaviour have been investigated, and one commercially-produced electrodeposited coating characterized. The quality of the coatings was assessed using the coincident site lattice model to analyse the properties of the grain boundaries. For cold spray coatings the grain size and number of coincident site lattice grain boundaries increased, and plastic strain decreased, with carrier gas velocity. In all cases annealing improved the quality of the coatings by increasing texture and coincidence site-lattices, but also increased the number of physical voids, especially when a low temperature cold spray carrier gas was used. Comparatively, the average grain size and number of coincident site-lattices was considerably larger for the strongly textured electrodeposited coating. Tensile testing showed the electrodeposited coating was much more strongly adherent to the steel substrate.

© 2015 Elsevier B.V. All rights reserved.

1. Introduction

The currently accepted approach to the long-term management of Canada's used nuclear fuel is Adaptive Phase Management (APM), which includes the option of sealing the used nuclear fuel in metal containers emplaced in a suitably selected deep geological repository (DGR) [1]. The current container design consists of a steel vessel (Canada) or cast iron insert (Sweden, Finland) with an external copper (Cu) shell which acts as a corrosion barrier. Following an early brief emplacement period, during which the containers will be warm due to radiation decay within the spent fuel, and oxygen trapped during emplacement activities will cause some corrosion, the repository conditions will be cool and humid or wet and anaerobic [2]. As a consequence, Cu is an ideal container material since it is thermodynamically stable under these anaerobic conditions [3]. Many archaeological (i.e., anthropogenic) and natural (i.e., natively formed metallic) artefacts confirm this stability [4,5].

To date, the majority of Cu container research has been on wrought Cu, of the form that can be readily manufactured into cylindrical components via extrusion, pierce and draw, and roll-forming methodologies [6–9]. However, for a dual-walled Cu-steel/cast iron container, ongoing manufacturing challenges exist, despite the fabrication of prototypes by Posiva (Finland) [10,11] and SKB (Sweden) [12]. To achieve sufficient structural support and ideal (i.e., round and non-ovalic) shape, both during and after manufacturing, cylindrical components must be significantly oversized and machined down extensively. An approximate additional 40% of the finished container weight must be removed and recycled in this process, even for a finished product that has a 5 cm final wall thickness. A further complication is the need to avoid long-term creep after emplacement within the DGR which requires tight machined tolerances between the inner vessel and outer shell; i.e., a nominal gap of <1.5 mm over the full container length (>4 m).

---

* Corresponding author.
 E-mail address: dwshoesm@uwo.ca (D.W. Shoesmith).

To overcome these issues, Cu coated steel containers are being investigated by the Nuclear Waste Management Organization (NWMO, Toronto Ontario, Canada). The coatings would be formed directly on the surface of the steel vessel with a thickness defined by the need for corrosion protection. Recent calculations [13,14] suggest a corrosion allowance of only 1.27 mm would be required to prevent failure by corrosion under the conditions anticipated in a DGR.

The use of commercial processes, such as cold spray coating and electrodeposition are being considered [15,16]. Cold spray coating is a material deposition process that accelerates small (approximately 10−100 μm in diameter) un-melted powders to high velocities (500−1200 m/s) using a supersonic jet gas stream [17,18]. The low applied temperatures and short applied time scales limit oxidation and changes in the physical properties of the feedstock particles making cold spray coating an attractive option compared to other commonly used thermal spraying techniques. However, as produced, the resultant Cu coating is expected to have significant residual cold work, with additional hardness and a low fracture toughness. These properties can be altered to produce a more conventional form of Cu by post-deposition annealing at moderately low temperatures (i.e., 300−400 °C) [19].

To justify the adoption of such a technology for used-fuel containers the microstructural features of the coatings and the quality of the interface between the Cu and the steel vessel must be evaluated. Electron Back-Scattered Diffraction (EBSD)—a technique that has been adopted as a standard for determining grain sizes [20]—and electron microscope imaging techniques have been applied to determine grain size, orientation and texture, as well as the distribution of strain within the coatings and across the Cu/steel interface. This study is part of an ongoing program to evaluate the viability of different coating processes [15,21,22] by determining the most cost-efficient coating parameters (i.e., spraying temperature, pressure and carrier gas), and their mechanical properties and degradation (corrosion) rates. The application of EBSD will help to optimize the choice of coating parameters required to satisfy mechanical design requirements and to identify the microstructural features which could be important in determining corrosion rates. A detailed study of the corrosion performance of these coatings are published elsewhere [23].

2. Experimental

2.1. Cold spray Cu feedstock powders

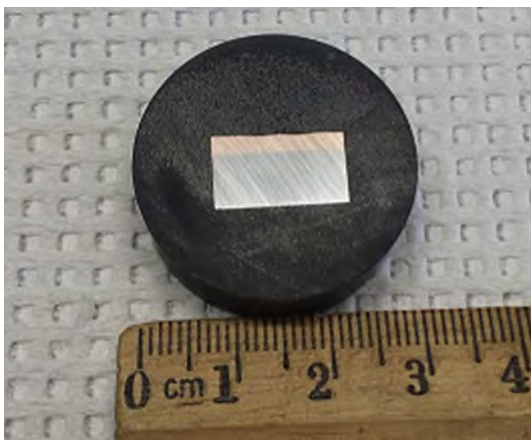Commercially available Cu feedstock powders (Inovati,

Fig. 1. Photograph of a typical Cu coating cross-section used for microscopy analyses.
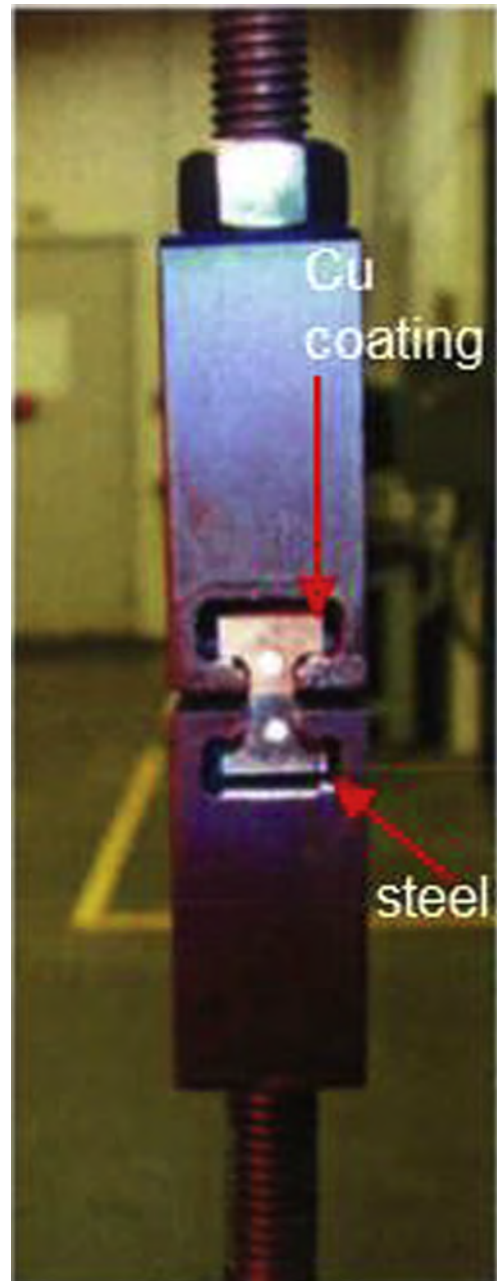

Fig. 2. Modified test jig used to mount and apply tensile stresses to Cu coating/steel substrates (courtesy of NWMO and Exova).

KMCu−HC) used in the production of the cold spray coatings were supplied by the National Research Council (NRC), Boucherville, Québec. Nominally, the Cu particles have a diameter between 5 and 20 μm and contain a low oxygen content of 0.190 ± 0.004%. To facilitate their characterization, these powders were stirred and mounted in a mixture of carbon fibres and Struers EpoFix®resin and hardener to form a black solidified epoxy disc with a diameter of 2.5 cm. Carbon fibres were used to mitigate charging caused by the electron beam used in EBSD measurements. One face of the disc surface was prepared for EBSD measurements using the procedure described in Section 2.4.

2.2. Cu cold spray coatings

Cu cold spray coatings (3 mm (0.118″) thick) on 6.35 mm (¼″)

thick mild steel plate were coated and supplied by the National Research Council (NRC), Boucherville Québec. Cylinders were machined from the plates, and a further coating applied to the exposed substrate sides. Prior to Cu cold spray deposition, the mild steel substrate was degreased with alcohol, and then grit blasted with 24 grit alumina. To determine the effect of the cold spray carrier gas and sprayed powder velocity (v), three cold spray coatings, formed at $v_{300\ °C,\ 4\ MPa}$, $v_{600\ °C,\ 5\ MPa}$ and $v_{800\ °C,\ 5\ MPa}$, were compared. Coatings formed at $v_{300\ °C,\ 4\ MPa}$ were sprayed with a Kinetiks™ 4000 cold spray system using the KMCu−HC powders in the carrier gas helium (He). The latter two coatings were formed using a PCS−1000 system (Plasma Giken Co. Ltd., Japan) using larger Cu powders (40−50 μm) and two carrier gases; He to bond and coat the initial ~ 100 μm, followed by nitrogen (N_2) to develop the final coating thickness. It has been demonstrated that the use of He leads to better coating-substrate bonding [15], while the use of the less-expensive N_2 improves cost-efficiency. Measured average powder velocities, during application of the N_2 layer were 695 ± 170 m/s and 637 ± 137 m/s for cold spray temperature and pressure conditions of $v_{800\ °C,\ 5\ MPa}$ and $v_{600\ °C,\ 5\ MPa}$, respectively [21]. Cold spray velocities were not measured for the $v_{300\ °C,\ 4\ MPa}$ condition. The effect of annealing was investigated by applying a 4 h, 400 °C, post-coating heating using an Argon (Ar) cover gas.

2.3. Electrodeposited Cu/mild steel substrates

Integran Technologies Inc. supplied Cu coatings on mild steel substrates formed by electrodeposition from a Cu^{2+} solution [22]. While some details of the coating process are proprietary, it can be noted that pyrophosphate constituents were used to maintain high Cu purity, and pulsed electrodeposition procedures were employed. The finished coating thickness was approximately 3 mm, following some surface preparation to remove slight surface roughness post electrodeposition.

2.4. Sample preparation for EBSD measurements

Cu coated steel rods were cut transversely into smaller rectangular pieces. Fig. 1 shows a photograph of a typical cross-section used for microscopic analyses. Cross-sectioned specimens were mounted in a mixture of Struers EpoFix® resin and carbon fibres. After grinding up to 2400 grit with SiC papers, the cross-section was polished using a 3 μm diamond abrasive and an ethanol/propanol lubricant. To minimize thick scratches produced by grinding and polishing the Cu portion of the cross-section was swabbed and etched with a 1:1:1 volume ratio mixture of 3% hydrogen peroxide, ammonium hydroxide, and water. The specimen was then finally polished with a 1 μm diamond abrasive and ethanol/propanol lubricant, followed by vibratory polishing on a Buehler Vibromet® II loaded with a 1:1 volume ratio mixture of 0.04 μm colloidal silica and ethylene glycol. The polished sample was rinsed and sonicated with acetone, and then with ethanol/propanol. Non-conductive organic solvents were used throughout the polishing stages to avoid steel corrosion caused by the galvanic coupling of the dissimilar metals.

2.5. Electron beam imaging, EBSD, and EDX measurements

A Hitachi SU6600 field emission scanning electron microscope was used to record electron micrographs and perform EBSD
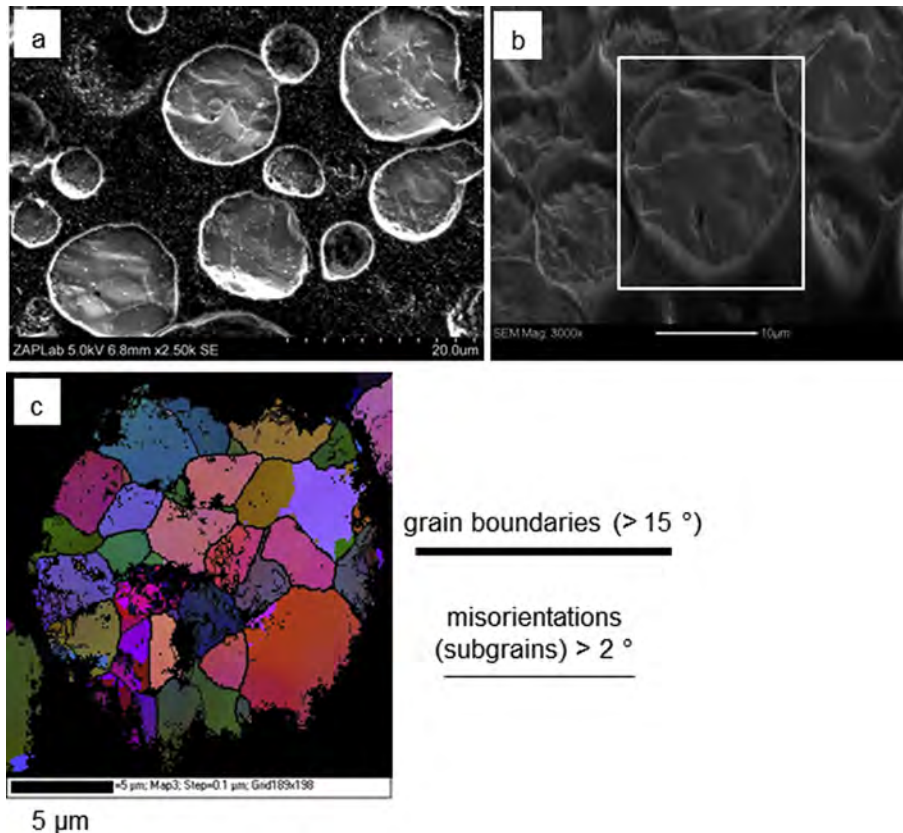

Fig. 3. (a) SE micrograph of the cold spray Cu powder mounted in a carbon fibre/epoxy mixture. (b) SE micrograph of a tilted Cu powder surface to be used for EBSD measurements; (c) Euler contrast EBSD map of the Cu powder. The indexing rate, including voids within the powder was >80%.

measurements. To image and enhance contrast between grain structures, a five segment solid-state back-scatter detector was used while applying a low (5 kV) beam voltage and slightly tilting the sample with a low working distance. Energy Dispersive X-Ray (EDX) spectroscopic measurements on Cu coated regions were recorded with an Oxford Instruments X-Max 80 mm^2 silicon drift detector and analysed with INCA Energy Software. EBSD maps of a 55 μm × 30 μm area were recorded with an Oxford Instruments Nordlys EBSD detector at a step size of 150 nm, with an applied voltage and current of 20 kV and 8 nA, respectively. The mounted cross-section was tilted at 70° and raised to a working distance of 19 mm. Oxford HKL Channel 5 EBSD software suite and the provided crystallographic references (i.e., fcc Cu and bcc iron (Fe)), were used to index diffraction band centres with 5−7 Kikuchi bands and a Hough Transform resolution of 80 and 4 × 4 binning.

2.6. EBSD data processing

EBSD maps were processed with an Oxford HKL Channel 5 EBSD Tango software module. No post-data noise reduction was applied to any of the data sets. For EBSD measurements on the cold spray coatings, non-indexed points can be just as informative as indexed points because they provide information on coating porosity and the presence of voids and nanocrystalline features. Grains were defined as domains that differ in adjacent crystallographic orientation by ≥ 15°; this delineation defined the grain boundary (high angle) regions. Coincidence Site Lattices (CSLs) were defined by the Brandon criterion [24]. Types of grain boundaries, i.e., Coincidence Site Lattices (CSLs) were noted in the legend to each EBSD map. The orientation resolution of the EBSD camera is generally <0.5°, making misorientations >2° within grains significant and usable to identify the location of misorientations (plastic strain). EBSD local misorientation maps, using a 3 × 3 kernel average algorithm, were produced for the Cu coatings. The extent of misorientation, or subgrain features, within grains is used as an approximate measurement of plastic strain, and depending on the resolution and grain size, may also be used as a measure of dislocation density [25]. Such measurements are limited, especially for the relatively smaller recrystallized cold spray grains, making a comparison between the Cu coatings mainly qualitative.
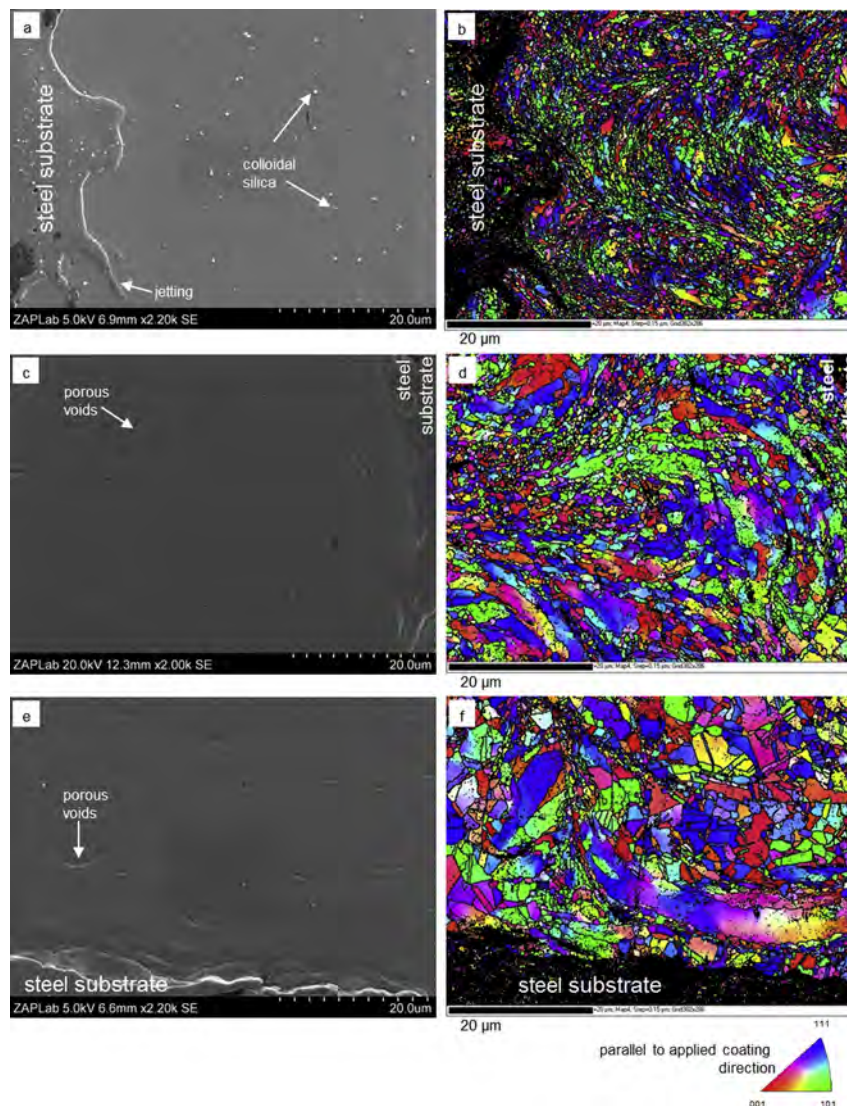
Fig. 4. Electron micrographs and corresponding EBSD IPF maps recorded at the Cu coating/steel interface: (a) and (b) cold-sprayed at $v_{300\ °C,\ 4\ MPa}$: (c) and (d) cold sprayed at $v_{600\ °C,\ 5\ MPa}$: (e) and (f) cold sprayed at $v_{800\ °C,\ 5\ MPa}$. The indexing rates were 68%, 78% and 83% for (b), (d) and (f), respectively.

2.7. Adhesion strength testing

To assess coating adhesion, dog-bone coupons were machined by wire electric discharge machining (EDM) for tensile testing according to ASTM standard E8–08 [26]. A test jig, shown in Fig. 2, was modified to accommodate the Cu coated steel specimens (not the same dimensions used for microscopy). Jig fabrication, as well as sample preparation and testing, were performed at Exova (Cambridge, Canada).

3. Microscopy results

3.1. Feedstock Cu cold spray powders

Fig. 3a shows a Secondary Electron (SE) micrograph of mounted feedstock Cu cold spray powders distributed across an epoxy/carbon fibre surface. Powder diameters, consistent with measurements made by NRC-Boucherville [21], ranged from 10 to 40 μm, with an average diameter of approximately 13 μm. Fig. 3b shows an SE micrograph of the Cu powder tilted with respect to the electron beam normal and eventually subjected to EBSD measurements; the square white outline delineates the area mapped by EBSD. Fig. 3c shows the Euler angle (colour) contrast EBSD map of the Cu powder. Euler maps show primary colour variations within the Cu powder particles indicating that the individual particles are polycrystalline aggregates. Large voids are present within individual particles, especially along the grain boundaries. An appreciable degree of misorientation (>2°) is observed across isolated, larger grains suggesting that the feedstock powder inherited strain from the fabrication process.

3.2. Cold spray and cold spray annealed Cu coatings

3.2.1. Cu coatings cold sprayed at $v_{300\ °C,\ 4\ MPa}$, $v_{600\ °C,\ 5\ MPa}$, and $v_{800\ °C,\ 5\ MPa}$

Fig. 4 a–f show electron micrographs and corresponding EBSD maps recorded at the carbon steel/Cu coating interface for three different cold spray conditions. The micrographs reveal that the polished Cu coating surface is nearly scratch-free, but contained residual colloidal silica particles (confirmed by EDX) from the final polishing step (indicated by white spots on the micrographs). EDX analyses confirmed that no elements other than Cu and traces of oxygen (O) were detected between clean (silica free) grains and grain boundaries. A curved and physically deformed steel substrate was formed for all three conditions by the high-velocity impact—known as 'jetting' [27]—of feedstock powders on the substrate surface.

To assess the bonding quality and nature of any Cu recrystallization during the cold spray process, Inverse Pole Figure (IPF) maps were produced (Fig. 4b, d, and f) to analyse the distribution of crystallographic orientations (i.e., texture) in a section perpendicular to the steel substrate surface. IPF maps are referenced in parallel with respect to the indicated flow impact direction. Noticeable on the IPF maps, especially for coatings sprayed at $v_{300\ °C,\ 4\ MPa}$, Fig. 4a and b, are the effects of particle impact and direction identified by the concave (relative to the impact direction) swirl patterns defined by curvi-planar boundaries shared by multiple grains. Coatings formed at higher cold spray velocities lead to larger, rectangular shaped grains with a bimodal grain structure characterized by fine interconnected grains between much larger grains. IPF maps confirm that no significant texture was observed for all these cold spray conditions.

Misorientation maps of the regions shown in Fig. 4, were produced to determine whether distinct sub-grain (plastic strain) features spread laterally across the Cu particle bonding interfaces into the interior of the grains, as well as along the bonding interface towards the elongated grain region. Coatings formed under all three conditions showed many sub-granular structures, and more plastic strain than within the grains of the feedstock Cu powder. This observation confirms that shear straining, and eventual shear instabilities leading to the thermal softening of grains (i.e., grain shapes conforming to flow impact direction), occurs during
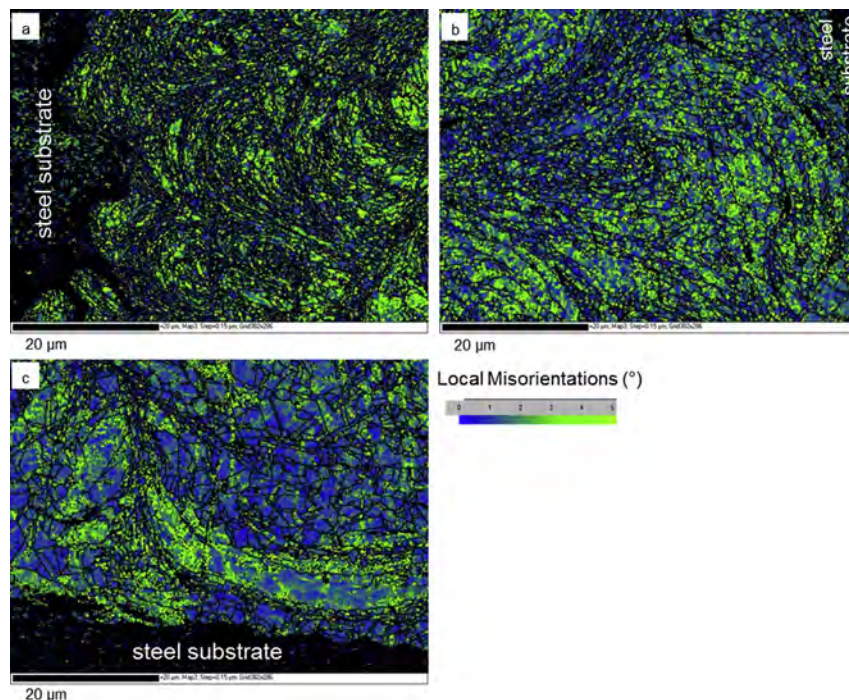

Fig. 5. Misorientation (plastic strain) maps produced for Cu-coating/steel interfaces cold-sprayed at (a) $v_{300\ °C,\ 4\ MPa}$, (b) $v_{600\ °C,\ 5\ MPa}$, and (c) $v_{800\ °C,\ 5\ MPa}$.

powder impact and bonding [28,29]. Taking into account these bonding mechanisms, individual grains formed at $v_{300\ °C,\ 4\ MPa}$ (Figs. 4b and 5a) were inspected to determine if the distribution of misorientations was influenced by impacting particles. Mostly random misorientations were observed throughout the grain features, including the curved regions, and no distinctive trend could be observed. The majority of the non-indexed points were concentrated near the grain boundary interfaces which were shown on SE micrographs to be continuous surfaces (i.e., not non-indexed regions caused by pits or scratch-induced relief). This indicates the presence of very small, possibly nanocrystalline features likely due to dislocations smaller than the 60 nm resolution of the EBSD system. These features are consistent with Transmission Electron Microscopy (TEM) analyses of various cold sprayed materials found in literature [19,30—32]. Further studies of the particle—particle bonding interfaces are planned at higher resolutions (i.e., <150 nm) to examine the bonding nature at low spraying velocities.

Cu grains formed at $v_{600\ °C,\ 5\ MPa}$ (Fig. 4d) still conformed to the flow impact direction and contained a substantial degree of plastic strain, albeit less than those deposited at $v_{300\ °C,\ 4\ MPa}$ (Fig. 4b) suggesting that, although flow stresses were still high, thermal softening was becoming dominant over shear straining at higher impact velocities. In addition to thermal softening, recrystallization of Cu cold sprayed grains appeared to occur at $v_{600\ °C,\ 5\ MPa}$, and was likely the dominant process contributing to the larger more regularly (equiaxed) shaped grains formed at $v_{800\ °C,\ 5\ MPa}$ (Fig. 4f). The effects of the kinetic energy of the sprayed Cu powders on coating deposition quality have been explored [33—35] and confirm that the measured average velocities (695 m/s and 637 m/s) [21] for the two spray conditions using larger Cu-powders, satisfy the modelled [33,35] and experimentally-verified [34] critical powder velocities

necessary for minimal bonding. Moreover, the models for the evolution of temperature at shear interfaces [33,35] indicate that temperatures sufficient to melt Cu (melting point 1085 °C) would have been approached or exceeded at the two highest spray temperatures $v_{600\ °C,\ 5\ MPa}$ and $v_{800\ °C,\ 5\ MPa}$. This is consistent with our observations of an increased rate of recrystallization (Fig. 4) and relative decrease in plastic strain (Fig. 5) at the velocities achieved at these two temperatures (637 m/s and 695 m/s, respectively). That such elevated temperatures are approached/exceeded for only a very brief period is also consistent with the significant residual cold work and brittle quality of the as-deposited cold spray coatings. Extremely little ductility is observed in tensile test measurements (i.e., <1%, Table 2, below); thus recrystallization during deposition is limited to a very limited period. Misorientations (sub-grains) associated with the most intense cold spray conditions (Fig. 5c) are concentrated at regions where the smallest grains are interconnected between larger grains, providing further supporting evidence that recrystallization is dominant at $v_{800\ °C,\ 5\ MPa}$ since sub-grain coalescence is a well known pre-cursor and nucleation site for recrystallization [36].

Although EBSD indexing rates—which may be considered a measure of deposition quality—increased with increasing impact velocities, larger, non-indexed porous voids were also observed at higher velocities. Their presence, as black areas on SE micrographs, suggests they may be porous regions caused by erosion [34,35] rather than nano-crystalline features undetected at the resolution achieved.

Using He as a carrier gas, rather than the heavier N_2, is known to lead to higher transport velocities of the Cu particles leading to enhanced adhesion. To optimize production costs without compromising the quality of the substrate/coating interface, coatings were formed at $v_{600\ °C,\ 5\ MPa}$ and $v_{800\ °C,\ 5\ MPa}$ using He gas for
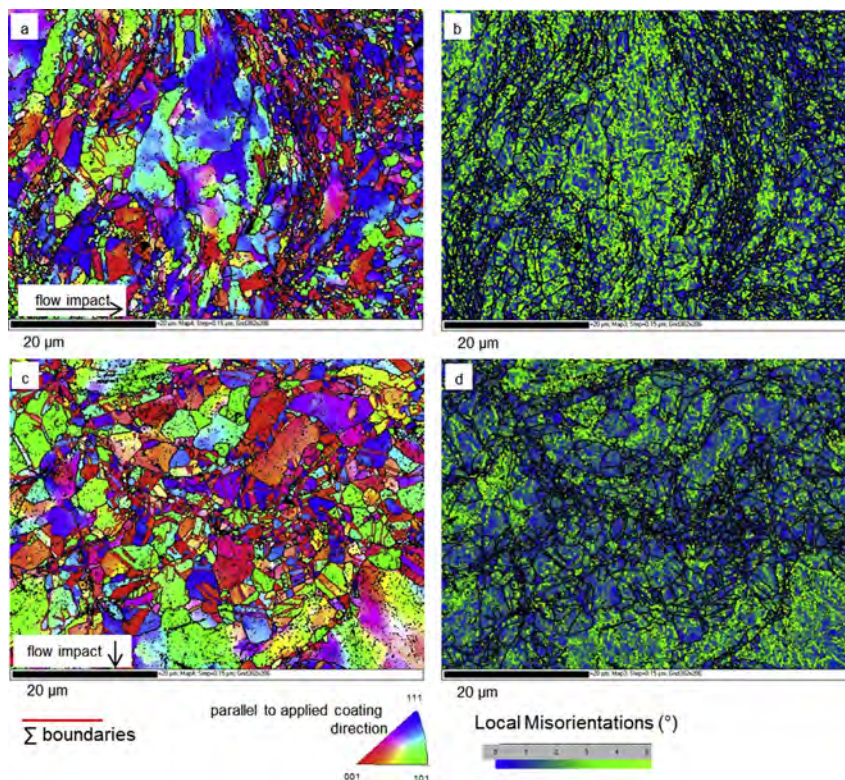

Fig. 6. EBSD IPF maps and corresponding strain maps produced for regions where the cold spray carrier gas was switched from He to N_2 for spray conditions of (a, b) $v_{600\ °C,\ 5\ MPa}$ and (c, d) $v_{800\ °C,\ 5\ MPa}$. The indexing rates were 85% and 83%, respectively.

the initial ~100 μm, and then developed to the desired thickness using N$_2$. Fig. 6a and b shows IPF maps and the respective strain maps recorded for such coatings. No significant differences in grain size, or bonding quality were observed for the bulk coating layers compared to the copper/steel interfaces.

3.2.1.1. Annealed Cu cold spray coatings. Annealing cold spray coatings is intended to enhance their ductility. The effect of annealing on re-crystallization was investigated by heating samples to 400 °C for 4 h. Fig. 7 shows IPF maps and matching SE micrographs for the three different Cu coatings after annealing. The most drastic change in recrystallization was observed for the coating formed at the lowest velocity $v_{300 °C, 4 MPa}$, Figs. 4b and 7b, with the average grain size quadrupling after annealing. However, a bimodal grain structure was obtained with grains <1 μm in dimension, concentrated at distances <2 μm from the steel substrate and nearby by large void regions (seen as non-indexed black areas). By contrast, recrystallized regions away from voids and the Cu/steel interface exhibited grains up to 6 μm in dimension. Smaller Cu grain sizes concentrated along the steel interface were also observed for the other spray conditions $v_{600 °C, 5 MPa}$ (Fig. 7d) and

$v_{800 °C, 5 MPa}$ (Fig. 7f—only a small portion of the substrate shown). However only minor voids were observed after annealing for the higher spray velocities.

The formation of small voids after annealing appears to be a common problem with commercial cold spray materials [37,38]. The origin of these voids is not understood but the observation that the regions in which they occur are inter-connected and contribute to a bi-modal grain structure suggests they are sites of ineffective recrystallization. It is notable that non-indexed locations in the EBSD maps align with the physical voids marked in the SE images. There are significantly fewer void regions observable in the SE image than indicated in the EBSD maps, and the voids do not appear to be connected. For all sprayed conditions, annealing decreased the plastic strain (strain maps were compared but are not shown for annealed coatings) confirming enhanced ductility.

The IPF maps in Fig. 7 show that annealing leads to some texture development along the <001> and <111> directions, especially for the larger grains. Overlaid on the IPF maps are Coincidence Site Lattices (CSLs). The CSL model defines grain boundary geometry based on the degree of coincident lattice sites between adjacent grains and follows a reciprocal notation: i.e., a Σ 5 boundary
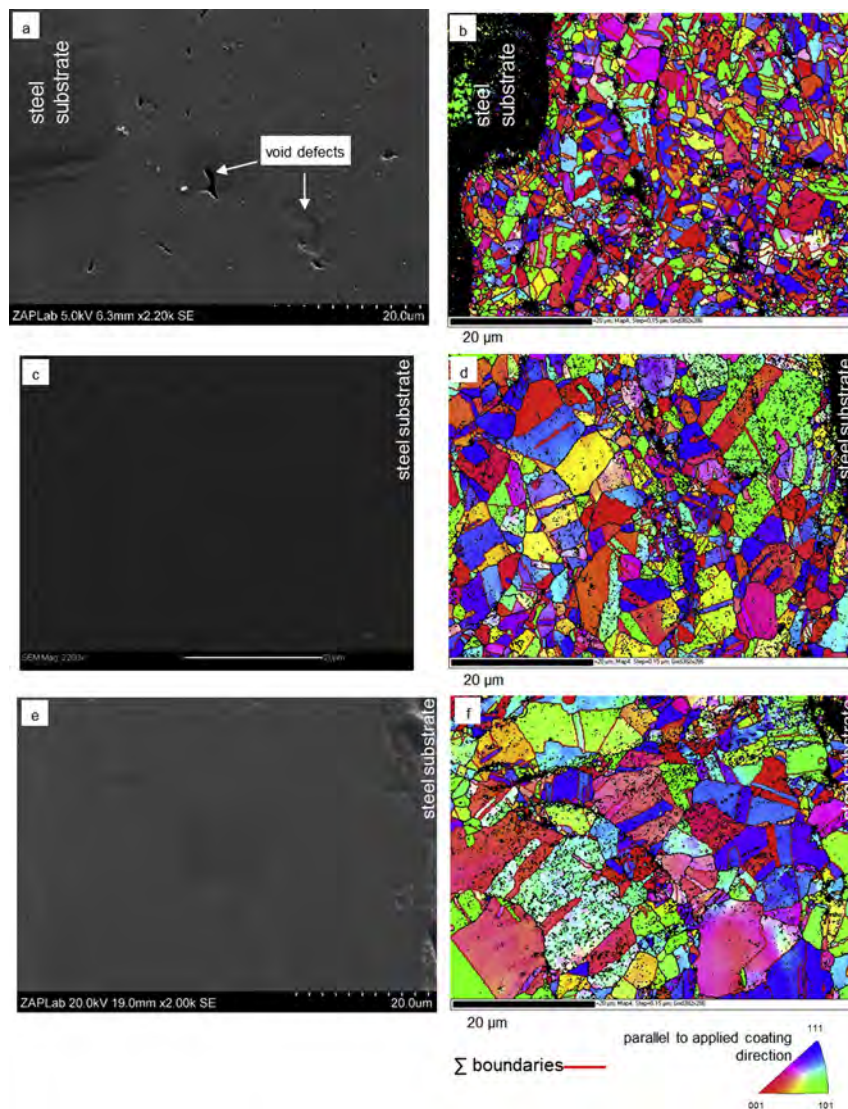
Fig. 7. EBSD IPF maps and corresponding SE micrographs of post-annealed (4 h, 400 °C) Cu coatings formed with cold spray conditions (a, b) $v_{300 °C, 4 MPa}$, (c, d) $v_{600 °C, 5 MPa}$ and (e, f) $v_{800 °C, 5 MPa}$; the indexing rates were 83%, 84%, and 84%, respectively.
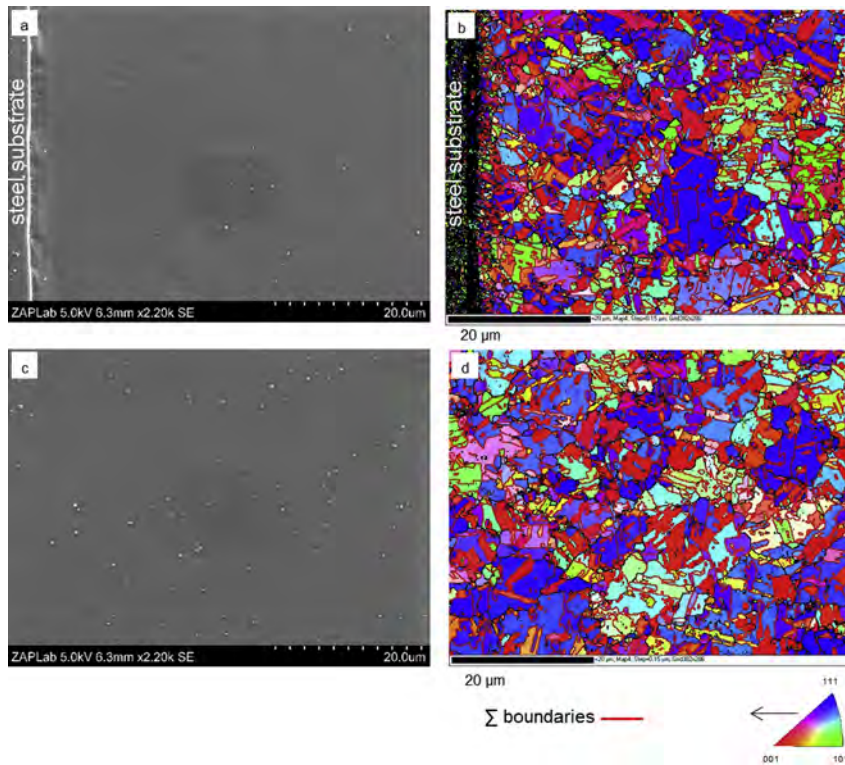
Fig. 8. SE micrographs recorded at (a) the electrodeposited Cu/mild steel interface and (c) near the middle of the electrodeposited Cu coating layer: (b) and (d) are EBSD IPF maps of the areas shown in (a) and (c) respectively: the indexing rates were 90% and 92% for 8b and 8d, respectively.
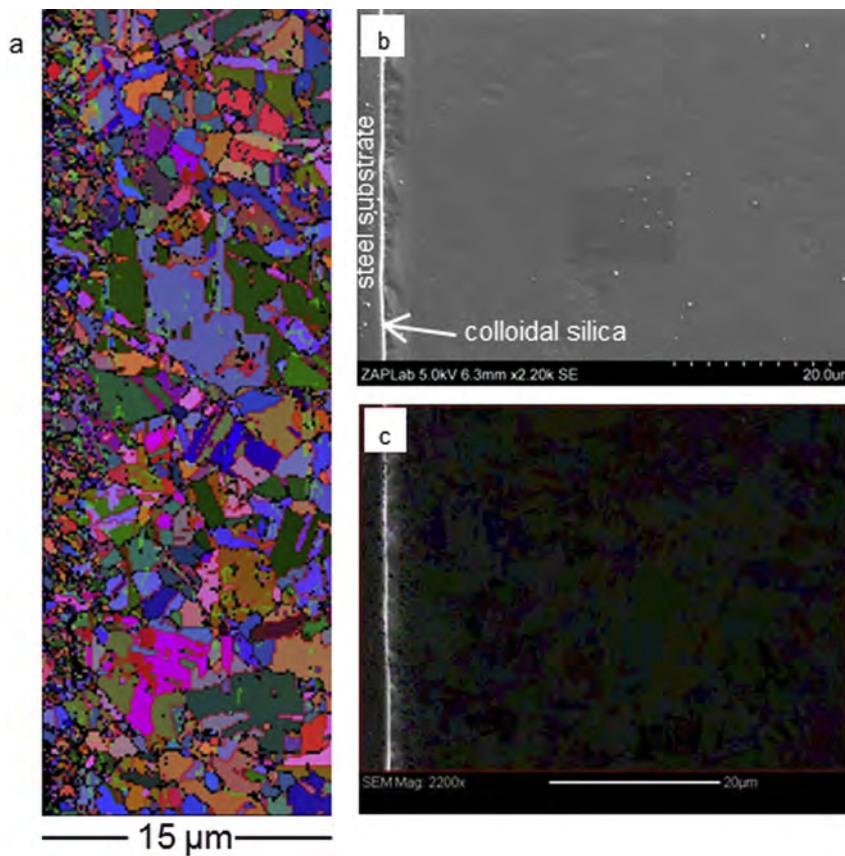
Fig. 9. (a) Euler map (6 μm × 25 μm) of electrodeposited Cu grains adjacent to the steel substrate: (b) and (c) show a SE micrograph and Euler colours index overlaid on the micrograph, recorded at the steel/electrodeposited Cu interface, respectively.

exhibits coincidence for 1/5 of the lattice points [39]. $\sum$ values ≤ 29, designated 'special' boundaries, are well known to possess extraordinary properties compared to high angle 'random' boundaries [40], including a greater resistance to corrosion [41,42]. The number and type of CSL boundaries provides some indication of the effectiveness of the recrystallization process. Annealing leads to recrystallization of the cold sprayed grains into grains with a greater number of CSLs, primarily $\sum 3$ grain boundaries. $\sum 3$ boundaries may also be twin boundaries exhibiting angle/axis boundary geometry 60°/<111>. Distinct twinning is apparent within some of the larger grains for all three of the spray conditions, Fig. 7. The largest increase in CSL boundary length due to annealing, 30%, occurred for the coating sprayed at the lowest velocity compared to 23% and 3% for the higher velocities, $v_{600\ °C,\ 5\ MPa}$ and $v_{800\ °C,\ 5\ MPa}$, respectively. Overall, the annealed coating formed at $v_{800\ °C,\ 5\ MPa}$ contained the greatest percentage of $\sum$ boundary lengths. The minimal effect of annealing on grain properties for coatings formed at $v_{800\ °C,\ 5\ MPa}$ supports the claim recrystallization was dominant at the highest spray velocity and lead to stable grain structures subsequently apparently unaffected by the annealing process.

The increase in CSLs during recrystallization is significant considering wrought Cu is not known to twin to the same extent as other Face-Centred Cubic (fcc) structures like nickel (Ni). While further investigations are required to define the recrystallization mechanism, there are many features within the grains formed at lower spraying velocities that have been reported to contribute and favour effective recrystallization. These include grain boundary anisotropy and curvature, and extensive sub-grain networks that would favourably coarsen into larger grains during annealing [43,44].

3.3. Electrodeposited Cu coatings on mild steel

Fig. 8 shows SE micrographs and corresponding IPF maps recorded at the electrodeposited Cu/steel interface (Fig. 8a and b) and within the bulk of the Cu coating (Fig. 8c and d). Compared to the cold spray coatings average Cu grain sizes are considerably larger (9 μm) and strongly textured along the <111> direction normal to the coating direction and outer surface. A contributing factor to this texturing is the high number of CSL boundaries (red on IPF maps) which make up close to 40% of the grain boundary length; i.e., 10% more than for the annealed cold spray coatings formed at $v_{800\ °C,\ 5\ MPa}$. Despite effective crystallization throughout the bulk coating, the electrodeposited grains nearest the steel substrate were noticeably smaller than those in the bulk coating.

This is well illustrated in the rectangular Euler map of the electrodeposited Cu grains nearest the steel substrate, Fig. 9a. In addition, a SE micrograph, Fig. 9b, and a Euler map with an overlaid micrograph, Fig. 9c, of the interface show that the majority of non-indexed points close to the interface could not be attributed to residual colloidal silica left behind on the interface by the polishing procedure. Closer examination along the interface, Fig. 9b, reveals that the Cu coating in contact with the steel alloy is significantly rougher than that away from the substrate. Moreover, Fig. 9c shows this interfacial region did not diffract indicating an amorphous coating. Further support that recrystallization was limited at the interface is indicated by the Euler map in Fig. 9a for the initial 3 μm thick crystallized region which shows the grains within this region are smaller (average grain size < 3 μm), and contain a greater density of voids (index rate = 70%) compared to the coating further from the steel substrate (index rate = 91%). It is possible that crystallization at the interface is limited because the coating layer thickness (i.e., <3 μm) is less than the effective grain size. Presently it is unclear to what extent the steel alloy surface impacts nucleation and growth of electrodeposited Cu grains.

3.4. Cu-coating adhesion testing

Tables 1 and 2 list the results of tensile tests and the location of the eventual fracture for the electrodeposited specimen and a non-annealed cold spray specimen coated at $v_{300\ °C,\ 4\ MPa}$, respectively.

Given the microstructural observations discussed above, a comparison between the lowest velocity cold spray coating and the electrodeposited coatings would be the most extreme. On average, electrodeposited coatings withstood 4 × the tensile load of the cold spray coating and fractured within the bulk coating, as opposed to the cold spray coating which fractured at the coating/steel interface. Since both coatings showed grain properties to be different within the first few microns beyond the steel substrate, the enhanced interfacial resistance to the tensile load for electrodeposited coatings is likely a result of the physicochemical bonding properties established during coating. However, it should be noted that the adhesion strengths measured for the cold spray coatings still exceeded, by considerable margins, the preliminary performance requirement of 8 MPa, and the preliminary design requirement of 20 MPa. The annealed cold spray coatings would be expected to have even greater adhesion strengths.

4. Summary and conclusions

Three different cold spray coatings, formed using He and N_2

Table 1
Tensile test results for 15 electrodeposited Cu-coatings (courtesy of NWMO and Exova).

Specimen dimensions (mm)	0.20% Offset yield load for gauge length of 5.9 mm (MPa)	Ultimate tensile stress (MPa)	Elongation in 5.90 mm gauge length (%)	Fracture location
4.38 × 4.13	289.7	351.0	57	Copper
5.07 × 4.14	303.5	351.1	50	Copper
4.49 × 4.13	300.4	307.4	1.0	Copper near interface
5.04 × 4.09	303.2	350.3	56	Copper
5.02 × 4.12	n/a	197.3	n/a	Copper near interface
4.85 × 4.13	267.6	271.6	9.5	Copper near interface
4.95 × 4.09	296.9	348.7	51	Copper
4.97 × 4.11	299.1	350.5	52	Copper
4.96 × 4.09	295.3	348.5	48	Copper
5.01 × 4.13	302.1	351.4	49	Copper
4.92 × 4.09	297.2	351.3	50	Copper
4.51 × 4.13	301.7	351.1	50	Copper
4.95 × 4.09	304.8	353.2	51	Copper
4.97 × 4.08	301.8	350.6	48	Copper
4.91 × 4.12	304.5	312.4	21	Copper near interface

Table 2
Tensile test results for 15 cold spray Cu-coatings (courtesy of NWMO and Exova).

Specimen dimensions (mm)	0.2% Offset yield load	Ultimate tensile stress (MPa)	Elongation in 5.90 mm (%)	Fracture location
5.03 × 4.00	n/a	82.5	n/a	Interface
5.08 × 4.03	n/a	100.6	n/a	Interface
5.09 × 4.01	n/a	85.2	n/a	Interface
5.02 × 4.01	n/a	124.2	n/a	Interface
5.07 × 4.03	n/a	71.9	n/a	Interface
5.04 × 4.00	n/a	82.8	n/a	Interface
5.14 × 4.04	n/a	83.8	n/a	Interface
5.05 × 4.01	n/a	97.3	n/a	Interface
4.44 × 4.05	n/a	76.7	n/a	Interface
5.07 × 4.00	n/a	73.5	n/a	Interface
4.26 × 4.05	n/a	85.8	n/a	Interface
4.32 × 4.05	n/a	61.2	n/a	Interface
4.99 × 4.01	n/a	76.5	n/a	Interface
4.66 × 4.05	n/a	73.7	n/a	Interface
5.02 × 4.00	n/a	73.7	n/a	Interface

carrier gases at different temperatures and pressures (i.e., different powder velocities) and a commercially-produced electrodeposited coating have been characterized.

For cold spray coatings the microstructure and strain density varied with coating conditions. At low cold spray velocities shear straining and limited recrystallization lead to grain shapes which conform to the flow impact direction. At higher temperatures thermal softening lead to more efficient recrystallization and larger more equiaxed grains.

Annealing decreased the plastic strain leading to recrystallization to larger grains and an improvement in ductility, but also to the development of some physical voids especially for coatings formed at lower deposition velocities.

The effectiveness of the annealing process was assessed by determining the length of coincident site lattice boundaries before and after annealing with the biggest improvement being achieved for the coating formed at lower temperatures. The minimal observable improvement due to annealing for the coating formed at the higher temperature can be attributed to effective recrystallization already realized during the coating process itself.

Average grain sizes for the electrodeposited coating were considerably larger than for the cold spray coatings. The high number of coincident site lattice boundaries confirmed the presence of effective crystallization.

Electrodeposited coatings withstood much higher tensile loads. The eventual failure of the cold spray coating occurred at the coating/steel interface while for the electrodeposited coating failure occurred in the bulk of the coating confirming the stronger adhesion of the coating to the substrate.

For both coatings the adhesion strength exceeded the preliminary design requirements.

Acknowledgements

References

[1] Implementing Adaptive Phased Management 2013 to 2017, NWMO, Toronto, 2012.
[2] F. King, Overview of a Carbon Steel Container Corrosion Model for a Deep Geological Repository in Sedimentary Rock, TR-2007-01, NWMO, Toronto, 2007.
[3] M. Pourbaix, Atlas of the Electrochemical Equilibria, NACE, Houston, 1974.
[4] F. King, Appl. Geochem. 10 (1995) 477—487.
[5] F. King, L. Ahonen, C. Taxén, U. Vuorinen, L. Werme, Copper Corrosion under Expected Conditions in a Deep Geologic Repository, Swedish Nuclear Fuel and Waste Management, 2001. TR 01-23, Stockholm.
[6] J. Smith, Z. Qin, F. King, L. Werme, D.W. Shoesmith, Corrosion 63 (2007) 135—144.
[7] J. Chen, Z. Qin, D.W. Shoesmith, J. Electrochem. Soc. 157 (2010) C338—C345.
[8] F. King, C. Lilja, M. Vähänen, J. Nucl. Mater. 438 (2013) 228—237.
[9] I. Betova, M. Bojinov, C. Lilja, Corros. Sci. 76 (2013) 192—205.
[10] H. Raiko, Disposal Canister for Spent Nuclear Fuel—Design Report, Posiva, Olkiluoto, 2005, 2005—02.
[11] Posiva, Expected Evolution of a Spent Nuclear Fuel Repository at Olkiluoto; 2006—05, Posiva, Olkiluoto, 2006.
[12] Svensk Kärnbränslehantering AB, Fuel and Canister Process Report for the Safety Assessment SR-can, SKB, Stockholm, 2006. TR 06-22.
[13] G.M. Kwong, Status of Corrosion Studies for Copper Used Fuel Containers under Low Salinity Conditions, NWMO, Toronto, 2011. Report NWMO TR-2011-14.
[14] J.R. Scully, M. Edwards, Review of the NWMO Copper Corrosion Allowance, NWMO, Toronto, 2013.
[15] P.G. Keech, Using copper coatings for corrosion protection of a used fuel container during geological storage, in: 14th International High-level Radioactive Waste Management Conference (IHLRWMC 2013): Integrating Storage, Transportation, and Disposal April 28—May 2, 2013, Albuquerque, New Mexico, USA. Paper # 6887, 2013.
[16] P.G. Keech, P. Vo, S. Ramamurthy, J. Chen, R.L. Jacklin, D.W. Shoesmith, Corros. Eng. Sci. Technol. 49 (2014) 425—430.
[17] A.P. Alkhimov, A.N. Papyrin, V.F. Dosarev, N.I. Nesterovich, M.M. Shuspanov. U.S. Patent 5, 302, 414, 1994.
[18] A.N. Papyrin, S. Klinkov, A. Alkhimov, V. Fomin, Cold Spray Technology, Elsevier, Amsterdam, 2007.
[19] P.D. Eason, J.A. Fewkes, S.C. Kennett, T.J. Eden, K. Tello, M.J. Kaufman, M. Tiryakioğlu, Mater. Sci. Eng. A 528 (2011) 8174—8178.
[20] ASTM Standard E04.11, Standard Practice for Determining Average Grain Size Using Electron Backscatter Diffraction (EBSD) in Fully Recrystallized Polycrystalline Materials, ASTM International, West Conshohocken, 2013, http://dx.doi.org/10.1520/E2627. www.astm.org.
[21] P. Vo, D. Poirier, J.-G. Legoux, P.G. Keech, E. Irissou, Application of copper coatings onto used fuel canisters for the Canadian nuclear industry, in: J. Karthikeyan, C. Kay (Eds.), Applications of High Pressure Cold Spray Technology, ASM International, Materials Park, Ohio, USA, 2015 (in press).
[22] K. Aust, I. Brooks, F. GonzalpaPosivatent, P. Lin, G. Palumbo, K. Tomantschger, N. Nagarajan. Integran Technologies, patent CA 2, 674, 403. 2009.
[23] R. Partovi-Nia, S. Ramamurthy, D. Zagidulin, J. Chen, R. Jacklin, P.G. Keech, D.W. Shoesmith, Corrosion (2015), http://dx.doi.org/10.5006/1757.
[24] D.G. Brandon, Acta Metall. 14 (1966) 1479—1484.
[25] S.I. Wright, M.N. Nowell, D.P. Field, Microsc. Microanal. 17 (2011) 316—329.
[26] ASTM Standard E8/E8M-08, Standard Test Methods for Tension Testing of Metallic Materials, ASTM International, West Conshohocken, 2008.
[27] M. Fukumoto, H. Terada, M. Mashiko, K. Sato, M. Yamada, E. Yamaguchi, Mater. Trans. 50 (2009) 1482—1488.

[28] H. Assadi, F. Gärtner, T. Stoltenhoff, H. Kreye, Acta Mater. 51 (2003) 4379–4394.
[29] T. Klassen, F. Gärtner, T. Schmidt, J.-O. Kliemann, K. Onizawa, K.-R. Donner, H. Gutzmann, K. Binder, H. Kreye, Mater. Werkst. 41 (2010) 575–584.
[30] P.D. Eason, T.J. Eden, S.C. Kennett, M.J. Kaufman, J. Powder Metall. Min. 1 (2012) 1–5.
[31] M.R. Rokni, C.A. Widener, V.R. Champagne, J. Therm. Spray. Technol. 23 (2013) 514–524.
[32] K. Kim, M. Watanabe, J. Kawakita, S. Kuroda, Scr. Mater. 59 (2008) 768–771.
[33] T. Schmidt, F. Gärtner, H. Assadi, H. Kreye, Acta Mater. 54 (2006) 729–742.
[34] T. Schmidt, H. Assadi, F. Gärtner, H. Richter, T. Stoltenhoff, H. Kreye, T.J. Klassen, Therm. Spray. Technol. 18 (2009) 794–808.
[35] H. Assadi, T. Schmidt, H. Richter, J.-O. Kliemann, K. Binder, F. Gärtner, T. Klassen, H. Kreye, J. Therm. Spray. Technol. 20 (2011) 1161–1176.
[36] F.J. Humphreys, M. Hatherly, Recrystallization and Related Annealing Phenomena, second ed., Elsevier, Amsterdam, 2004.
[37] Y. Zou, W. Qin, E. Irissou, J.-G. Legoux, S. Yuea, J.A. Szpunar, Scr. Mater. 61 (2009) 899–902.
[38] I. Smid, A.E. Segall, P. Walia, G. Aggarwal, T.J. Eden, J.K. Potter, Tribol. J. 55 (2012) 599–605.
[39] S. Ranganathan, Acta Cryst. 21 (1966) 197–199.
[40] G. Palumbo, K.T. Aust, Special properties of $\sum$ grain boundaries, in: D. Wolf, S. Yip (Eds.), Materials Interfaces, Chapman and Hall, London, 1992, pp. 190–211.
[41] P. Jakupi, J.J. Noël, D.W. Shoesmith, Electrochem. Solid-State Lett. 13 (2010) C1–C3.
[42] S.H. Kim, U. Erb, K.T. Aust, G. Palumbo, Scr. Mater. 44 (2001) 835–839.
[43] A.D. Rollet, J. Mater. 56 (2004) 63–68.
[44] N. Bozzolo, N. Souaï, R.E. Logé, Acta Mater. 60 (2012) 5056–5066.